



Dissolution of Glass–Ceramic Scaffolds of Bioactive Glasses 45S5 and S53P4

Laura Aalto-Setälä¹ · Minna Siekkinen¹ · Nina Lindfors² · Leena Hupa¹

Received: 22 October 2022 / Accepted: 19 December 2022 / Published online: 12 January 2023
© The Author(s) 2023

Abstract

Although the initial *in vitro* dissolution of bioactive glasses (BAG) is well characterized, the long-term behaviour of crystallized BAG scaffolds in a continuous fluid flow is incompletely understood. A detailed understanding of the long-term dissolution of scaffolds is vital for predicting their behaviour in clinical applications. Here, we explored the dissolution and reaction mechanisms of partly crystalline and glass–ceramic scaffolds based on the bioactive glasses S53P4 and 45S5 using a continuous flow-through method in Tris-buffer (Tris) and simulated body fluid (SBF) for up to 21 days. Granules of the parent glasses were used as references. The main crystalline phase in both scaffolds was sodium–calcium–silicate. The scaffolds' dissolution suggested that the sodium–calcium–silicate crystals dissolved incongruently to yield hydrous silica. The silica phase then provided abundant nucleation sites for hydroxyapatite precipitation, resulting in fine-grained crystalline structures. When exposed to Tris, the scaffolds almost completely dissolved within the test period, leaving only highly porous remnant phases. For the 45S5 scaffolds, the calcium phosphate reaction layers that formed on their surfaces effectively slowed the dissolution in SBF. In contrast, this effect was less apparent for the S53P4 specimens.

Keywords Bioactive glass · Crystallization · Scaffolds · Biomedical materials · Biodegradable materials · Dissolution behaviour · Continuous · Dynamic · Tissue engineering

Introduction

The dissolution of bioactive glasses (BAGs) determines their ability to produce therapeutic effects, stimulate tissue growth, and interact with cellular processes in bone tissue regeneration [1–3]. Improved understanding of the dissolution process is necessary to develop tissue-engineering scaffolds based on BAGs. Despite extensive research on the *in vitro* dissolution of BAGs in static [4–7], half-dynamic

[8], and closed circulation systems [9], knowledge on the reaction kinetics using continuous flow-through test methods is limited. Furthermore, previous studies have mainly focussed on glass powders or particles [10–15].

Ideally, a BAG dissolves at a rate comparable to tissue regeneration, thus providing space for neogenesis [16]. The biological reactions at the BAG lead to a dual-surface layer that chemically binds the BAG to tissue, especially to bone [3, 17]. The release of soluble silicate species and calcium ions from the BAG during dissolution induces osteostimulation [18–20]. Moreover, the gradual formation of a dual surface, consisting of an inner silica-rich and an outer crystalline hydroxyapatite (HA) layer, likely changes the dissolution kinetics of the glass, which also affects the biological response of the BAG [21].

When designing BAG-based implants for new medical applications, one major challenge is understanding the short- and long-term behaviour of the implant *in vivo*. Release of ions from the BAG to the surrounding solution should be sufficiently high to stimulate the cellular processes needed to support tissue regeneration or bacteriostasis [1, 22]. If HA deposition retards overall dissolution, ions released from

✉ Leena Hupa
leena.hupa@abo.fi

Laura Aalto-Setälä
laura.aalto-setala@lasifaasi.fi

Minna Siekkinen
minna.siekkinen@abo.fi

Nina Lindfors
nina.c.lindfors@hus.fi

¹ Johan Gadolin Process Chemistry Centre, Åbo Akademi University, Henrikinkatu 2, 20500 Turku, Finland

² Department of Hand Surgery, Helsinki University Hospital, University of Helsinki, PL 3, 00014 Helsinki, Finland

the BAG may decrease below the critical biological levels needed to support cellular processes. Conversely, a BAG that does not develop a suitably thick HA layer may dissolve too rapidly, making it an ineffective scaffold [21, 23].

BAGs are currently used primarily as granules in various bone-filling clinical applications [3]. Increased research is devoted to developing porous BAG-based scaffolds [24–35]. The strong crystallization tendency of two well-known commercial BAGs (45S5 and S53P4) limits their hot-working into amorphous scaffolds. Consequently, amorphous porous scaffolds from other glass compositions with relatively high silica content have been developed, allowing hot-working without crystallization [36, 37]. Interestingly, amorphous S53P4 scaffolds have recently been successfully sintered under carefully controlled conditions [38, 39].

Several variables affect the *in vivo* degradation behaviour of BAGs [40]. The dissolution of 45S5 and S53P4 depends on the location of the implant [41]. Unreacted 45S5 has been found several months after implantation in rabbit femurs [42]. Similar findings were reported for clinical studies of S53P4. In addition to anatomical location, bone remodelling also depends on the amount and particle size of the implanted BAG [41, 43]. Crystallization reduces the dissolution rate compared with the parent BAG [44, 45]. Understanding the detailed dissolution kinetics of partially crystallized S53P4 and glass–ceramic 45S5 scaffolds may aid in developing mechanically strong implants for load-bearing applications.

This work reports on the dissolution behaviour of crystalline and partially crystalline scaffolds of 45S5 and S53P4 BAGs using a continuous flow-through test method in simulated body fluid (SBF) and Tris for up to 21 days. The objective of this study was to assess the impact of crystallization on scaffold dissolution. The results provide insight into the reaction kinetics of these crystalline phases, which may lead to improved tissue-engineering scaffold designs with controlled degradation.

Materials and Methods

Scaffold Preparation

BAGS S53P4 and 45S5 were prepared by mixing appropriate amounts of Na_2CO_3 , $\text{CaHPO}_4 \cdot 2(\text{H}_2\text{O})$, CaCO_3 , and glass-quality Belgian quartz sand (Sigma-Aldrich, Steinheim, Germany). The batches were melted at 1360 °C in separate platinum crucibles for 3 h before casting the glass into a block-form graphite mould. For homogeneity, the glasses were melted twice and crushed between melts. After casting, the glass blocks were annealed at 520 °C for 1 h before the annealer was allowed to cool. The nominal oxide compositions of 45S5 and S53P4 are shown in Table 1. The annealed

Table 1 Nominal oxide compositions of BAGs 45S5 and S53P4 in wt% (mol%)

Glass	SiO_2	Na_2O	CaO	P_2O_5
45S5	45.0 (46.1)	24.5 (24.3)	24.5 (26.9)	6.0 (2.6)
S53P4	53.0 (53.9)	23.0 (22.7)	20.0 (21.8)	4.0 (1.7)

blocks were crushed and sieved to yield granules between 300 and 500 μm . These granules were filled into separate cylindrical graphite moulds ($\text{Ø}5 \times 10$ mm) and sintered at 720 °C (S53P4) and 1030 °C (45S5) in nitrogen for 90 min to form porous scaffolds. Based on prior studies [46, 47], the sintering temperature of the S53P4 BAG was chosen to yield a partially crystallized scaffold that was strong enough for handling. The sintering temperature for the 45S5 BAG was higher because it does not form an adequate glass–ceramic scaffold below 1000 °C [47, 48].

In Vitro Dissolution Setup

The *in vitro* dissolution of the glass granules, crushed scaffolds, and sintered scaffolds was studied in continuous flow-through reactors. Simulated body fluid (SBF) and Tris-buffer (Tris) were continuously fed through the samples at an average flow rate of 0.2 mL/min. Fagerlund et al. described the reactor cell configuration in detail [12]. The flow rate was assumed to mimic the typical laminar flow of extracellular fluid in the human body [13]. SBF was prepared according to the protocol developed by Kokubo et al. [49]. Tris (50 mM, Trizma base, Sigma-Aldrich) was adjusted with 1 M HCl (J.T. Baker) to a pH of 7.40 at 37 °C.

The mass of the S53P4 granules and scaffolds varied from 270 to 300 mg. Dissolution tests with the more rapidly dissolving 45S5 granules and scaffolds were performed using smaller samples, ranging from 195 to 230 mg. The smaller 45S5 specimens ensured ion release in concentrations sufficiently low to prevent blockage. HA deposition within the reactor tubes was noted in preliminary tests when larger 45S5 masses were used.

The dissolution characteristics of granules and crushed scaffolds were analysed for 14 days. Sintered scaffolds were evaluated for 21 days. Solution temperatures were maintained at 37 °C.

The solution volume fed through the samples was measured at each time point. For each experiment, three discrete samples were sequentially collected at 15-min intervals every 1 to 3 days for up to 21 days. These samples were subsequently analysed for the amount of released inorganic ions. Then, once the total solution volume and the measured ions at each timepoint were known, an estimation of the amount of dissolved elements at each timepoint t was determined as a mean of the three consecutive measurements,

$$n_i(t) = \frac{1}{3} \sum_{j=1}^3 c_{ij} V_j(t) \tag{1}$$

where c_i is the measured concentration (mg/L) of element i , and $V(t)$ is the volume of the sample. The pH was also measured at each time point. When estimating the cumulative overall dissolution of each element, ion release between two consecutively measured time point was assumed as a mean of the two values. The dissolved fraction of element i cumulated until each time point t can then be written as

$$D_{ik}(t) = D_{ik}(t - 1) + \frac{n_i(t - 1) + n_i(t)}{2} \frac{V(\Delta t)}{x_i m_k} 100\% \tag{2}$$

where $D_i(t-1)$ is the dissolved fraction of element i determined at the previous measurement point, $V(\Delta t)$ is the measured volume of solution between the current time point and the previous measurement, x_i is the weight fraction of the element i in the glass, and m_k is the total original mass of the sample k .

Released ion concentrations were analysed using an inductively coupled plasma optical emission spectrometer (ICP-OES, Optima 5300 DV; Perkin Elmer, Waltham, MA). Before analysis, the solutions were diluted 1:10 using ultrapure water. The analysed elements included silicon ($\lambda = 251.611$ nm), calcium ($\lambda = 317.933$ nm), and sodium ($\lambda = 589.592$ nm). Phosphorus concentrations were too low to provide reliable data after the first few test days. Thus, phosphorus was omitted from the analyses. Calibration of the spectrometer was conducted using ultrapure water and multielement standards (Perkin Elmer Multi-Element Standard 25; silicon standard from Ultra Scientific) with 1 ppm Si, Ca, and Na. The calibration was reverified after every 20 samples. All values were background corrected. Due to the breakage of several 45S5 scaffolds when they were initially

inserted into the reactor cells ($\varnothing 5 \times 11$ mm), larger diameter reactor cells ($\varnothing 5.7 \sim 5.8$ mm) were used for subsequent specimens.

Scaffold and Granule Analyses After Immersion

After the in vitro experiments, the remaining scaffold pieces and granules were rinsed with ethanol to terminate the reactions, dried, weighed, and cast into epoxy resin. The resin-embedded samples were polished to reveal cross-sections of the reaction layers. The thickness and composition of the reaction layers were examined with a scanning electron microscope (SEM, Leo Gemini 1530, Carl Zeiss, Oberkochen, Germany) equipped with an energy dispersive X-ray analyser (EDX, UltraDry X-ray detector, Thermo Fisher Scientific, MA, USA).

The crystallized surface layer to the amorphous core ratio was identified from seven cross-sectional scaffold SEM panorama images for each S53P4 sample using image-analysis software (Photoshop CS6, Adobe Systems, Inc, San Jose, CA, USA). The percentage of the crystallized layer was then calculated from manipulated images by comparing the number of pixels in crystalline and amorphous areas. The amount of the crystalline and glassy phases in the thin crystallized layer was also calculated from 10 cross-sectional SEM images (5 k magnification), as described above.

Results

Ion Release

The concentrations of silicon released in both solutions and sodium and calcium released in Tris from S53P4-based samples are shown in Fig. 1. The phosphorus concentration

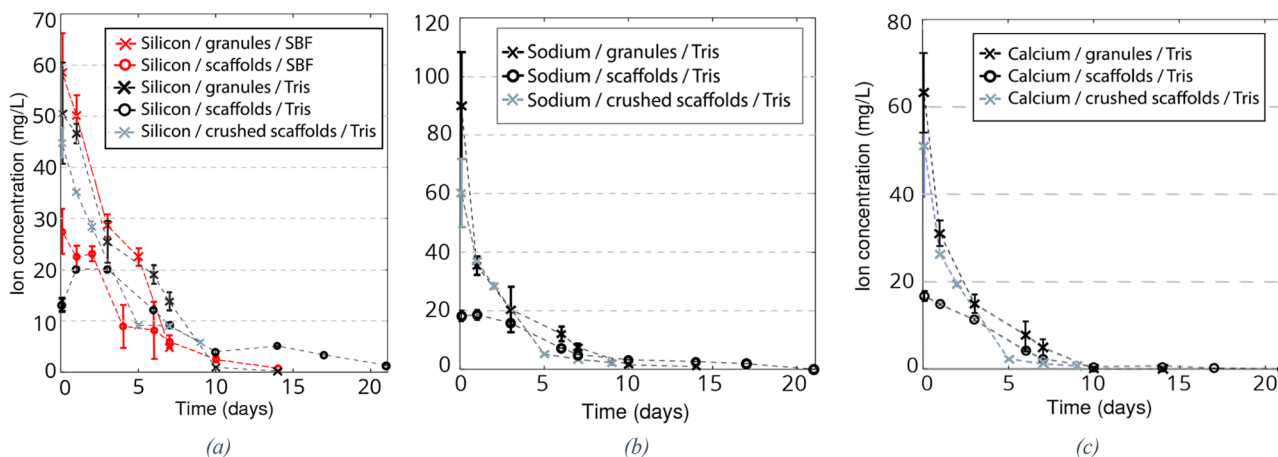


Fig. 1 Concentrations of ions released from S53P4 granules, scaffolds, and crushed scaffolds into the continuous flow of Tris and SBF: **a** Si in Tris and in SBF, **b** Na in Tris, and **c** Ca in Tris. Dashed lines provide visual guidance only

was close to the limit of quantification (LOQ). The corresponding ion concentrations released from 45S5-based samples are shown in Fig. 2. Although the initial ion concentrations released from the scaffolds were generally lower than those released from the glass granules, the differences diminished over time. After 21 days in continuous Tris flow, only a 1–3 mg remained of the amorphous S53P4 and 45S5 granules.

Sodium, calcium, and silicon species were released from the S53P4 scaffolds into Tris at measurable concentrations for 17 days. After longer periods, only the values for silicon were greater than the LOQ. The concentrations were lower for the scaffolds than granules for all elements, especially during the first days. There were no notable differences between the crushed scaffolds and the granules.

Despite its lower mass, the initial ion release was higher from the 45S5 samples than S53P4 samples. However, the

ion concentrations dissolving from 45S5 granules rapidly decreased after the initial peak. The released silicon concentration was higher from 45S5 scaffolds than from granules only for 1 day and 3 days for Na and Ca. The ion concentrations released from crushed 45S5 scaffolds were similar to the concentrations measured for granules. After 6 days in SBF, the ion concentrations dissolving from all 45S5 sample types also decreased below LOQ. In Tris, the concentrations for the crushed 45S5 scaffolds were below LOQ after 9 days. In contrast, the ion dissolution from 45S5 scaffolds was within the measurable range for 17 days.

The calculated cumulative dissolved fractions (calculated from Eqs. 1 and 2) of silicon for S53P4 and 45S5 samples are shown in Fig. 3. The last concentrations above the LOQ were measured at after 17 days after which the concentrations were below the LOQ for all measured elements. The values over 100% are considered due to having only a few

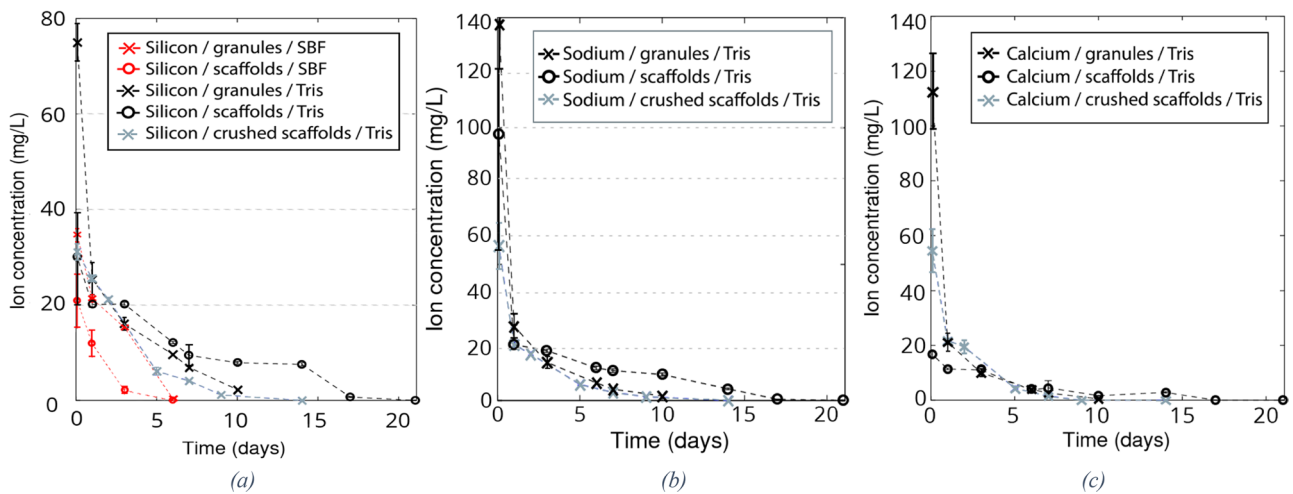
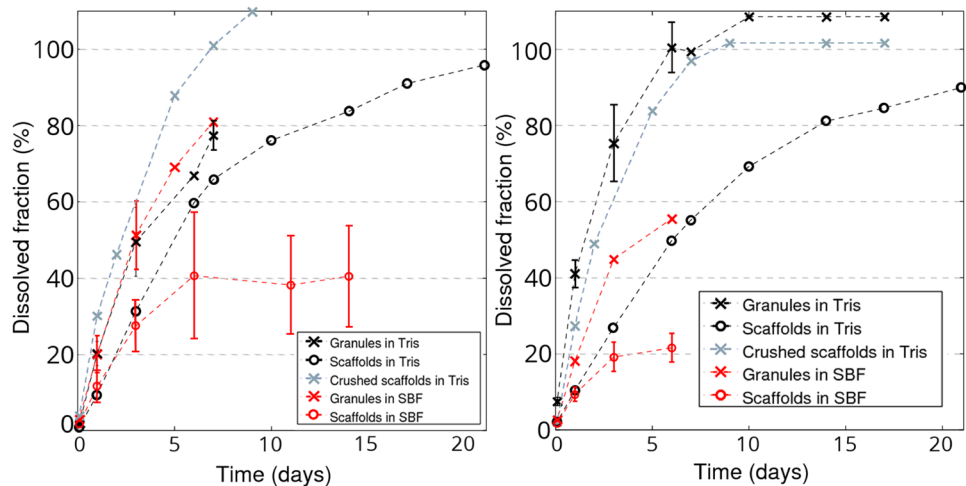


Fig. 2 Concentrations of ions released from 45S5 granules, scaffolds, and crushed scaffolds into continuous flow of Tris and SBF: **a** Si in Tris and in SBF, **b** Ca in Tris, and **c** Na in Tris. Lines provide visual guidance only

Fig. 3 Cumulative silicon dissolution of samples based on **a** S53P4 and **b** 45S5. Lines provide visual guidance only



measurement points during the initial diffusion-dominated phase of dissolution. The approximation here assumes the concentration between two consecutively measured time points as a mean of the two values.

The evolution of pH was examined throughout the dissolution (data not shown). The highest pH values, 7.81 for 45S5 granules and 7.72 for S53P4 granules, were measured at 60 min (the first measurement point). After 24 h, the pH decreased to 7.44 for S53P4 scaffolds and 7.58 for 45S5 scaffolds.

Scaffold Morphology Before Dissolution

According to SEM images and EDX analyses of S53P4 scaffolds, the crystallized surface layer appeared to contain a high share of amorphous phase, with more Si and less Na and Ca than the crystals. The calculated percentage of the phases in the manipulated (black and white colours) SEM image in Fig. 4b suggested $67 \pm 3\%$ (95% confidence level) crystals in the layer, with the remaining 33% being an amorphous phase. The thickness of the crystallized layer varied from 40 to 80 μm , depending on the measuring point in the scaffold. The smaller particles in the SEM image (Fig. 5) that suggest total crystallization were assumed to show the top or bottom cross-sections of the sintered granules in the scaffold and were thus disregarded in the thickness calculation. Figures 4b and 5 show that the crystallized surface layer covered $65 \pm 9\%$ (95% confidence level). Combining the thickness of the layer and its share of crystals yields an average of $44 \pm 6\%$ (95% confidence level) of crystals in the

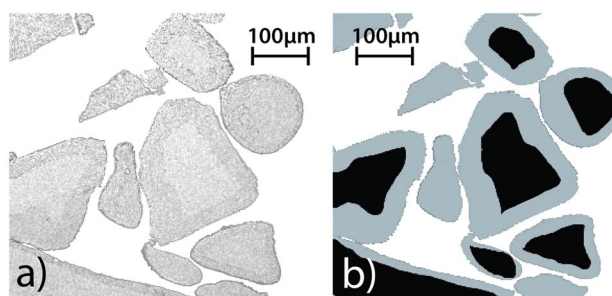


Fig. 5 a SEM image of S53P4 cross-section showing crystallized surface layer and amorphous cores b Manipulated SEM image showing the crystalline layer (grey) and amorphous cores (black)

cross-sectional area of sintered S53P4 scaffolds. Assuming spherical particles and their isotropic distribution, 58 vol-% of glass had crystallized. In contrast, the glass–ceramic 45S5 consisted of fine-grained crystals and a minor residual amorphous phase throughout the structure. Thus, similar estimations of the shares of the phases in 45S5 scaffolds could not be performed.

Reaction Layer Formation at Sample Surfaces

Figure 6 shows SEM analyses of S53P4 granule cross-sections after 14 days in continuous flow of Tris and 6 days in SBF. A silica-rich layer had formed on the granules in both solutions, but a calcium phosphate (CaP) layer could be identified only on granules exposed to SBF. The granules had dissolved to different extents in the two solutions. Some

Fig. 4 a SEM image and EDX line analysis along the arrow showing minor compositional differences between amorphous S53P4, crystals, and residual amorphous phase around the crystals. b SEM image of S53P4 scaffold showing crystals embedded in the amorphous phase (lower image) and a manipulated SEM image showing the residual amorphous (black) and crystalline (white) phases (upper image). The calculated amount of crystals in the SEM image is 62.5%

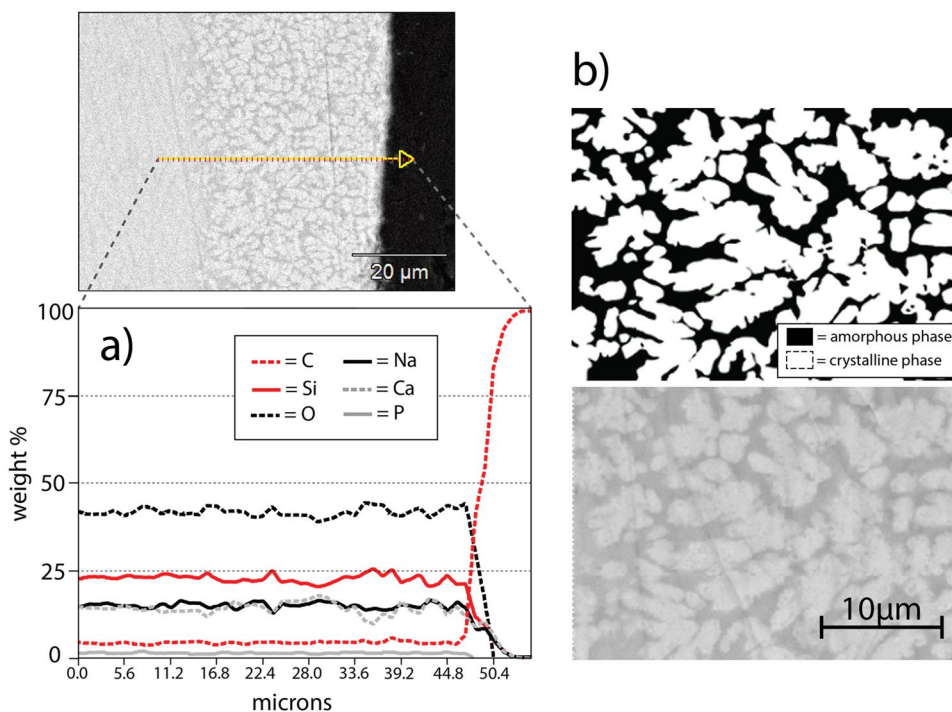
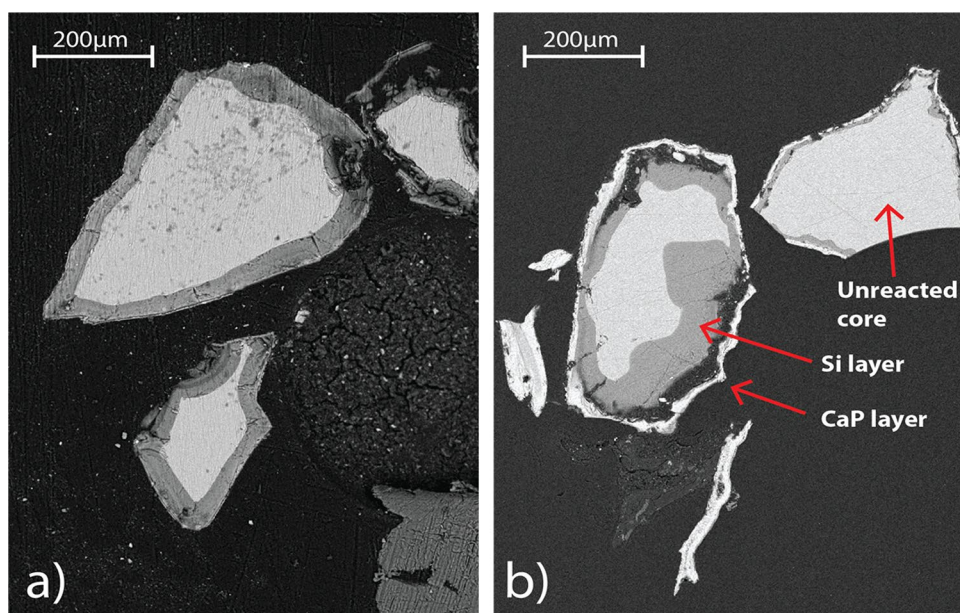


Fig. 6 SEM images of cross-sections of amorphous S53P4 granules after **a** 14 days in continuous flow (0.2 mL/min) of Tris and **b** 7 days in continuous flow (0.2 mL/min) of SBF



granules had dissolved almost entirely in Tris, whilst others still seemed intact after 14 days in Tris (Fig. 6a, b). All three S53P4-based specimens showed similar differences in degradation after the dissolution tests. After SBF dissolution, the shred-like CaP formations (Fig. 6b) were assumed to be CaP

reaction layers either left after the granules had dissolved or detached from the granule surfaces.

There was no observable CaP layer on S53P4 scaffolds after 21 days of continuous Tris flow (Fig. 7). The scaffolds had lost their structure due to degradation of the

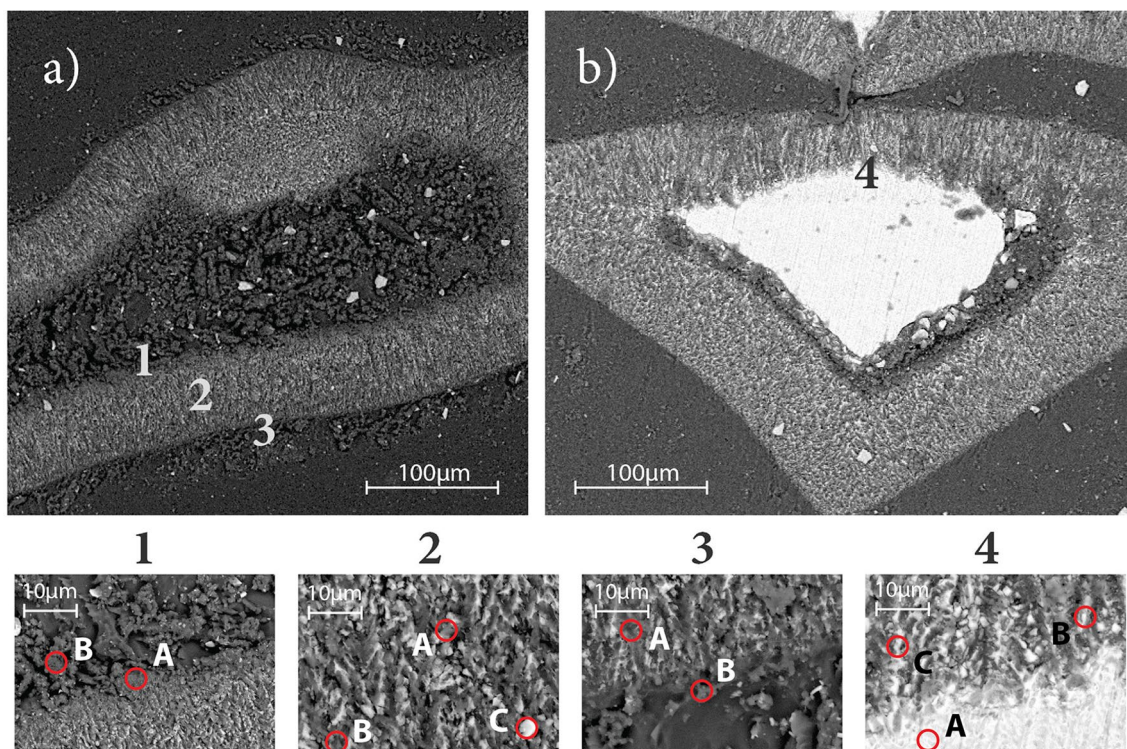


Fig. 7 SEM images of S53P4 scaffold remnant cross-sections after 21 days of dynamic Tris flow. **a** Granule-level detail of partly dissolved crystallized layer and almost completely dissolved core. **b**

Granule-level detail of partly dissolved amorphous core. EDX analyses of the points 1A-B, 2A-C, 3A-B, and 4A-C are shown in Table 2

Table 2 EDX analyses of points shown in Fig. 7

	SiO ₂	Na ₂ O	CaO	P ₂ O ₅
1A	93.4	1.0	1.8	0
1B	73.6	13.5	12.9	0
2A	91.1	0.3	6.8	1.0
2B	92.4	0	5.8	0.7
2C	99.0	0	1.0	0
3A	94.2	0	4.8	0
3B	45.2	28.1	26.7	0
4A	56.1	20.4	19.2	4.2
4B	87.9	2.6	7.8	1.0
4C	87.2	2.5	8.1	1.7

All values in wt%

necks between the granules. The most degraded scaffold granules also comprised of shells of the partly leached

crystallized surface layers (Fig. 7a). According to EDX analyses, these shells mainly consisted of silicon and oxygen, with minimal amounts of sodium and calcium in locations next to the granule core (Table 2).

After the dissolution of S53P4 scaffolds in SBF, a CaP-rich layer was identified on the outer surfaces and within the partly leached crystallized surface layer (Fig. 8a, b). The molar ratio Ca/P in the layer was close to 1.67 (i.e. the hydroxyapatite ratio). The amorphous cores of the scaffold granules started to dissolve during the experiments, as indicated by the gap between the core and outer CaP-rich surface layer (Fig. 8b).

There were thin CaP-rich surface films on the 45S5 scaffolds after 21 days in Tris (Figs. 9a, b). In contrast, the CaP layer formation was so extensive in SBF on glass 45S5 samples that the CaP layer connected granules after 7 days (Fig. 10b).

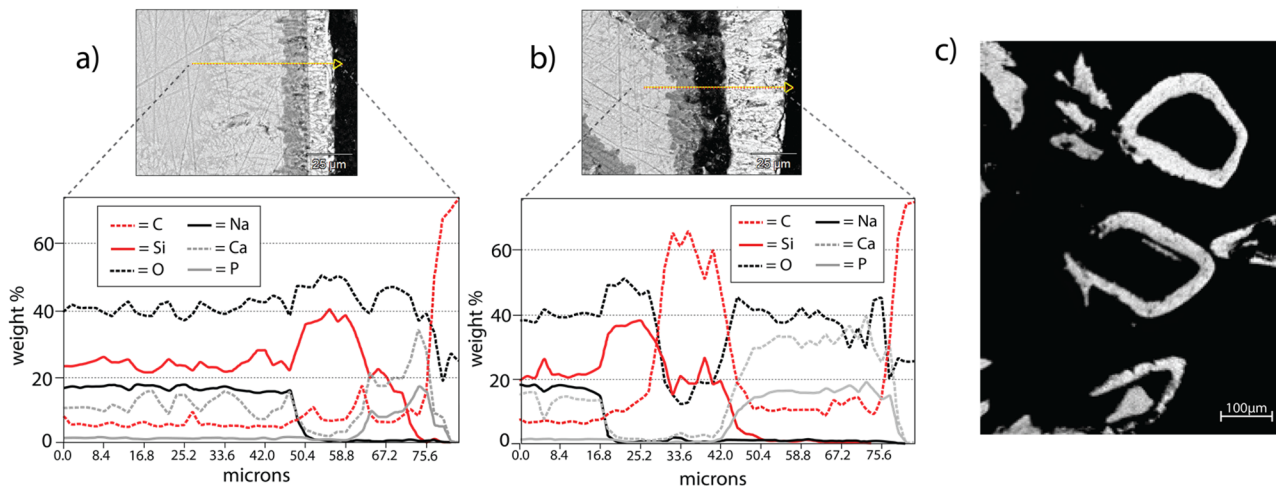


Fig. 8 SEM-EDXA of S53P4 scaffold after 14 days of continuous flow in SBF: **a** Reaction layer formation at the granule surface, **b** crystallized layer has formed CaP and the amorphous core has started to react, **c** granules with CaP surface layers left

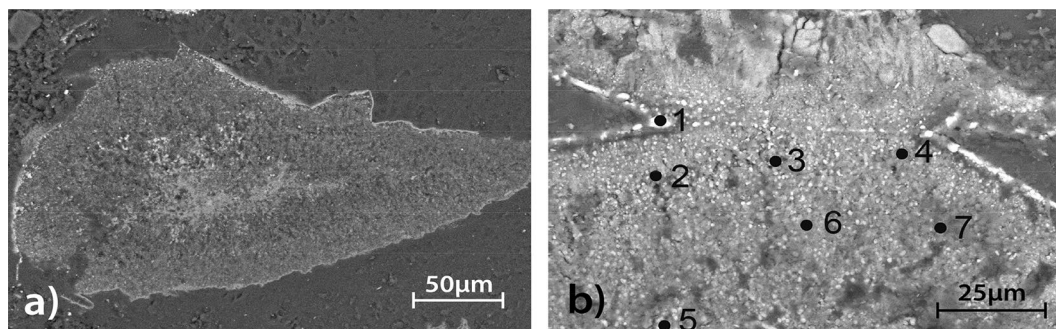
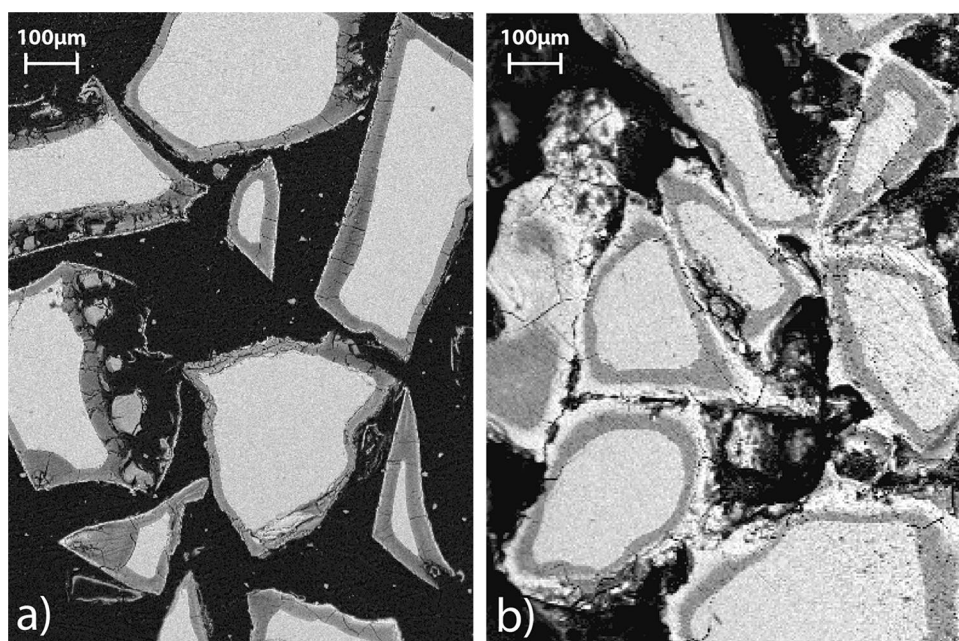


Fig. 9 SEM images of 45S5 scaffolds after 21 days in continuous flow of Tris: **a** Fine-grained structure showing various degrees of dissolution and reaction. **b** Higher magnification of the structure. EDX

analysis of the brighter coloured points 1, 2, 4, and 5 suggested Ca, P, and O, whereas the darker points 3, 6, and 7 consisted of Si, Na, Ca, O, and P

Fig. 10 Glass 45S5 granules after **a** 3 days in continuous flow (0.2 mL/min) of Tris and **b** 7 days in continuous flow (0.2 mL/min) of SBF. In the latter, the CaP formation (seen in white) has joined granules together. In the former, there is no considerable CaP layer but only a silica-rich layer (seen in dark grey)



Discussion

The degradation of porous S53P4 scaffolds with a crystallized surface layer and porous 45S5 glass–ceramic scaffolds was studied in continuous flow-through of Tris-buffer and SBF solutions for up to 21 days. The two BAGs exhibit different crystallization behaviours during sintering [46–48, 50]. Glass 45S5 exhibits bulk crystallization, with the primary crystalline phase $\text{Na}_2\text{CaSi}_2\text{O}_6$ precipitating at approximately 610 °C and the secondary phase $\text{Na}_2\text{Ca}_4(\text{PO}_4)_2\text{SiO}_4$ precipitating above 800 °C [48, 50]. 45S5 scaffolds sintered at 1030 °C consist of a fine-grained crystallized structure with a small residual glass share [51]. Glass S53P4 has a somewhat lower crystallization tendency than 45S5 and exhibits surface crystallization [46]. S53P4 can be sintered into amorphous or partially crystalline scaffolds under controlled conditions [38, 39, 47].

The *in vitro* degradation of the bioactive glass-based samples was studied in continuous fluid flow conditions to better mimic *in vivo* conditions than static *in vitro* tests. Further, feeding a fresh solution through the sample does not lead to saturation of the solutions [9, 12, 52, 53]. In static conditions, the solution saturation and high pH lead to extensive hydroxyapatite precipitation on the BAG, thus retarding the glass dissolution [54]. The overall validity of *in vitro* studies in SBF has been questioned during the past decade [53, 55], as highly reactive materials can exhaust the SBF solution in hours under static conditions. However, in a flow-through reactor setup the pH stays within the buffering range of the solution.

Silicate-based glasses have been studied under dynamic conditions for 30 min to four days [10–15]. The results are

consistent with those in this study: after an initial rapid burst, the dissolution changes into a more steady ion release. The initial ion release observed for all BAG-based samples is well established [7, 12, 13, 15, 56]. The initial rapid increase in pH might have contributed to the release of silicon species (Figs. 1 and 2). However, the highest solution pH values (7.7–7.8) did not exceed the buffering capacity of the solutions. Thus, the low network connectivity (NC), rather than hydrolysis of the Si–O–Si bonds in the glass structure contributed to the gradual degradation of the samples [57]. The calculated NC is higher for S53P4 than for 45S5 ($\text{NC}_{\text{S53P4}} = 2.54$; $\text{NC}_{45\text{S5}} = 2.12$), explaining the higher dissolution of Si from 45S5.

Overall, the amorphous granules dissolved more rapidly than crystallized scaffolds, which was observed in both solutions. Interestingly, ion dissolution from the amorphous granules and crushed scaffold particles of S53P4 and 45S5 exhibited no notable differences in Tris solution (Figs. 1 and 2). This indicates that the slower dissolution of scaffolds in Tris was mainly due to lower surface area and the different fluid flow paths through granules beds and porous structures.

In Tris, the crystallized structure of the scaffold particles did not prevent the dissolution, as almost all material dissolved. After 21 days of Tris solution immersion, only a small (1–3 mg) amount of material was left after the experiments. All material from amorphous granules was exhausted. Interestingly, very fragile, shell-like Si–O structures were left from the crystallized scaffolds of both glasses. This implies that the crystalline phases in 45S5 and S53P4 dissolved incongruently, releasing Na and Ca ions after the residual amorphous phase had leached out. This was observed by EDX analyses, showing only Si and O in

the most degraded sites of the structures. No XRD analyses could be performed to identify the phase compositions of the remnants, due to the small amount of material.

In SBF, the crystalline structures did not slow the formation of the HA layer. The SEM images showed CaP precipitation inside the crystallized surface layer for both glasses (Fig. 8), as also reported by Fagerlund et al. for glass S53P4 [46]. The HA layer was more extensive on the crystallized scaffold particles than on amorphous granules. This suggested that the leached crystallized layer provided a large number of nucleation sites for CaP precipitation. This led to a dense mixed layer that slowed (for glass S53P4) and stopped (for glass 45S5) the dissolution of the amorphous core. The differences between the two glasses were assumed to be due to their different phase compositions and crystal microstructures.

For S53P4, it is unclear, whether the ion-exchange reaction occurred primarily between Na^+ in the scaffold and H^+ in the solution or also with Ca^{2+} . The larger size of the calcium ions compared to sodium ions may retard their diffusion from the fine-grained 45S5 glass–ceramic structure. The observations of the 45S5 scaffold in SBF agree with the reported transformation of sodium–calcium–silicate crystals to amorphous calcium phosphate in vitro through a series of interactions between the crystals and solution [24, 31].

Our results show that despite the crystalline glass–ceramic structure, the dissolution continues until almost all material has been exhausted even though some remnant, highly porous phases were left. This implies that the remnant phases do not prevent the dissolution but provide nucleation sites for HA precipitation. These findings are important for future modelling of the crystallized BAG dissolution.

Conclusion

The long-term dissolution behaviours of sintered scaffolds of BAGs 45S5 and S53P4 were studied in continuous flow of Tris and SBF for up to 21 days. Amorphous granules of both glasses were used as references. S53P4 scaffolds consisted of granules with amorphous core and crystallized surface layers, whereas 45S5 scaffolds were throughout crystallized.

The crystallized layers dissolved incongruently. In Tris, the dissolution continued of crystallized S53P4 and 45S5 scaffolds until almost all material had been exhausted even though some remnant, highly porous phases were left. In SBF, the HA formation was more extensive on the leached crystalline surfaces than on the amorphous granules. The HA layer precipitated extensively inside the crystalline structure, whereas for the amorphous granule surfaces, the HA layer only precipitated on the granule surface. The remnant phases did not prevent the dissolution but provided more nucleation sites for HA precipitation.

The results suggested that the glass–ceramic specimens would fully dissolve with prolonged immersion time also in SBF, even though the solution pH values after the reactor did not markedly increase from the inflow values.

Acknowledgements The Graduate School of Materials Research at Åbo Akademi University is acknowledged for financial support of this work (Laura Aalto-Setälä). Financial support by Svenska Kulturfonden Project 157767 (Minna Siekkinen) is also acknowledged. Luis Bezerra and Linus Silvander are acknowledged for their technical assistance with ICP-OES and SEM.

Funding Open access funding provided by Abo Akademi University (ABO).

Declarations

Conflict of interest There are no conflict to declare.

Open Access This article is licensed under a Creative Commons Attribution 4.0 International License, which permits use, sharing, adaptation, distribution and reproduction in any medium or format, as long as you give appropriate credit to the original author(s) and the source, provide a link to the Creative Commons licence, and indicate if changes were made. The images or other third party material in this article are included in the article's Creative Commons licence, unless indicated otherwise in a credit line to the material. If material is not included in the article's Creative Commons licence and your intended use is not permitted by statutory regulation or exceeds the permitted use, you will need to obtain permission directly from the copyright holder. To view a copy of this licence, visit <http://creativecommons.org/licenses/by/4.0/>.

References

1. A. Hoppe, N.S. Güldal, A.R. Boccaccini, A review of the biological response to ionic dissolution products from bioactive glasses and glass-ceramics. *Biomaterials* **32**(11), 2757–2774 (2011). <https://doi.org/10.1016/j.biomaterials.2011.01.004>
2. A. Hoppe, V. Mouriño, A.R. Boccaccini, Therapeutic inorganic ions in bioactive glasses to enhance bone formation and beyond. *Biomater. Sci.* **1**(3), 254–256 (2013). <https://doi.org/10.1039/C2BM00116K>
3. J. Jones, D. Brauer, L. Hupa, D. Greenspan, Bioglass and bioactive glasses and their impact on healthcare. *Int. J. Appl. Glass Sci.* **7**, 423–434 (2016). <https://doi.org/10.1111/ijag.12252>
4. A.L. Maçon et al., A unified in vitro evaluation for apatite-forming ability of bioactive glasses and their variants. *J. Mater. Sci. Mater. Med.* **26**, 5403 (2015). <https://doi.org/10.1007/s10856-015-5403-9>
5. L. Varila, T. Lehtonen, J. Tuominen, M. Hupa, L. Hupa, In vitro behaviour of three biocompatible glasses in composite implants. *J. Mater. Sci. Mater. Med.* **23**(10), 2425–2435 (2012). <https://doi.org/10.1007/s10856-012-4693-4>
6. T.J. Lehtonen, J.U. Tuominen, E. Hiekkanen, Resorbable composites with bioresorbable glass fibers for load-bearing applications. In vitro degradation and degradation mechanism. *Acta Biomater.* **9**(1), 4868–4877 (2013). <https://doi.org/10.1016/j.actbio.2012.08.052>
7. M.G. Cerruti, D. Greenspan, K. Powers, An analytical model for the dissolution of different particle size samples of Bioglass® in TRIS-buffered solution. *Biomaterials* **26**(24), 4903–4911 (2005). <https://doi.org/10.1016/j.biomaterials.2005.01.013>

8. S. Radin, P. Ducheyne, S. Falaize, A. Hammond, In vitro transformation of bioactive glass granules into Ca-P shells. *J. Biomed. Mater. Res.* **49**(2), 264–272 (2000). [https://doi.org/10.1002/\(SICI\)1097-4636\(200002\)49:2%3c264::AID-JBM16%3e3.0.CO;2-2](https://doi.org/10.1002/(SICI)1097-4636(200002)49:2%3c264::AID-JBM16%3e3.0.CO;2-2)
9. P. Siriphannon, Y. Kameshima, A. Yasumori, K. Okada, S. Hayashi, Comparative study of the formation of hydroxyapatite in simulated body fluid under static and flowing systems. *J. Biomed. Mater. Res.* **60**(1), 175–185 (2002). <https://doi.org/10.1002/jbm.10056>
10. K. Schuhladen, X. Wang, L. Hupa, A.R. Boccaccini, Dissolution of borate and borosilicate bioactive glasses and the influence of ion (Zn, Cu) doping in different solutions. *J. Non-Cryst. Solids* **502**, 22–34 (2018). <https://doi.org/10.1016/j.jnoncrysol.2018.08.037>
11. L. Hupa, S. Fagerlund, J. Massera, L. Björkvik, Dissolution behavior of the bioactive glass S53P4 when sodium is replaced by potassium, and calcium with magnesium or strontium. *J. Non-Cryst. Solids* **432**, 41–46 (2016). <https://doi.org/10.1016/j.jnoncrysol.2015.03.026>
12. S. Fagerlund, P. Ek, L. Hupa, M. Hupa, Dissolution kinetics of a bioactive glass by continuous measurement. *J. Am. Ceram. Soc.* **95**(10), 3130–3137 (2012). <https://doi.org/10.1111/j.1551-2916.2012.05374.x>
13. S. Fagerlund, L. Hupa, M. Hupa, Dissolution patterns of biocompatible glasses in 2-amino-2-hydroxymethyl-propane-1,3-diol (Tris) buffer. *Acta Biomater.* **9**(2), 5400–5410 (2013). <https://doi.org/10.1016/j.actbio.2012.08.051>
14. M. Arango-Ospina, L. Hupa, A.R. Boccaccini, Bioactivity and dissolution behavior of boron-containing bioactive glasses under static and dynamic conditions in different media. *Biomed. Glas.* **5**(1), 124–139 (2019). <https://doi.org/10.1515/bglass-2019-0011>
15. D. Galuskova, H. Kaňková, A. Švančárková, D. Galusek, Early-stage dissolution kinetics of silicate-based bioactive glass under dynamic conditions: critical evaluation. *Materials* **14**, 3384 (2021). <https://doi.org/10.3390/ma14123384>
16. M.N. Rahaman et al., Bioactive glass in tissue engineering. *Acta Biomater.* **7**(6), 2355–2373 (2011). <https://doi.org/10.1016/j.actbio.2011.03.016>
17. L.L. Hench, R.J. Splinter, W.C. Allen, T.K. Greenlee, Bonding mechanisms at the interface of ceramic prosthetic materials. *J. Biomed. Mater. Res.* **5**(6), 117–141 (1971). <https://doi.org/10.1002/jbm.820050611>
18. L.L. Hench, Genetic design of bioactive glass. *J. Eur. Ceram. Soc.* **29**(7), 1257–1265 (2009). <https://doi.org/10.1016/j.jeurceramsoc.2008.08.002>
19. J. Jones, P. Sepulveda, L. Hench, Dose-dependent behavior of bioactive glass dissolution. *J. Biomed. Mater. Res.* **58**, 720–726 (2001). <https://doi.org/10.1002/jbm.10053>
20. I.D. Xynos, M.V.J. Hukkanen, J.J. Batten, L.D. Buttery, L.L. Hench, J.M. Polak, Bioglass (R) 45S5 stimulates osteoblast turnover and enhances bone formation in vitro: implications and applications for bone tissue engineering. *Calcif. Tissue Int.* **67**, 321–329 (2000)
21. W. Liang, C. Rüssel, D.E. Day, G. Völksch, Bioactive comparison of a borate, phosphate and silicate glass. *J. Mater. Res.* **21**(1), 125–131 (2006). <https://doi.org/10.1557/jmr.2006.0025>
22. V. Miguez-Pacheco, L.L. Hench, A.R. Boccaccini, Bioactive glasses beyond bone and teeth: emerging applications in contact with soft tissues. *Acta Biomater.* **13**, 1–15 (2015). <https://doi.org/10.1016/j.actbio.2014.11.004>
23. J. Massera, C. Claireaux, T. Lehtonen, J. Tuominen, L. Hupa, M. Hupa, Control of the thermal properties of slow bioresorbable glasses by boron addition. *J. Non-Cryst. Solids* **357**(21), 3623–3630 (2011). <https://doi.org/10.1016/j.jnoncrysol.2011.06.037>
24. F. Westhauser et al., Gelatin coating increases in vivo bone formation capacity of three-dimensional 45S5 bioactive glass-based crystalline scaffolds. *J. Tissue Eng. Regen. Med.* **13**(2), 179–190 (2019). <https://doi.org/10.1002/term.2780>
25. E. Boccardi et al., Bioactivity and mechanical stability of 45S5 bioactive glass scaffolds based on natural marine sponges. *Ann. Biomed. Eng.* **44**(6), 1881–1893 (2016). <https://doi.org/10.1007/s10439-016-1595-5>
26. E. Fiume, J. Barberi, E. Verné, F. Baino, Bioactive glasses: from parent 45S5 composition to scaffold-assisted tissue-healing therapies. *J. Funct. Biomater.* (2018). <https://doi.org/10.3390/jfb9010024>
27. F. Baino, E. Verné, C. Vitale-Brovarone, 3-D high-strength glass–ceramic scaffolds containing fluoroapatite for load-bearing bone portions replacement. *Mater. Sci. Eng. C* **29**(6), 2055–2062 (2009). <https://doi.org/10.1016/j.msec.2009.04.002>
28. F. Baino, E. Fiume, Elastic mechanical properties of 45S5-based bioactive glass-ceramic scaffolds. *Materials* **12**, 3244 (2019). <https://doi.org/10.3390/ma12193244>
29. F. Baino, E. Fiume, Mechanical characterization of 45S5 bioactive glass-derived scaffolds. *Mater. Lett.* **245**, 14–17 (2019). <https://doi.org/10.1016/j.matlet.2019.02.086>
30. A. Boccaccini, Q. Chen, L. Lefebvre, L. Gremillard, J. Chevalier, Sintering, crystallisation and biodegradation behaviour of bioglass-derived glass-ceramics. *Faraday Discuss.* **136**, 27–44 (2007). <https://doi.org/10.1039/B616539G>
31. D. Bellucci, V. Cannillo, A. Sola, An overview of the effects of thermal processing on bioactive glasses. *Sci. Sinter.* (2010). <https://doi.org/10.2298/SOS1003307B>
32. B. Thavornyutikarn, P.F.A. Wright, B. Feltis, W. Kosorn, T.W. Turney, Bisphosphonate activation of crystallized bioglass scaffolds for enhanced bone formation. *Mater. Sci. Eng. C* **104**, 109937 (2019). <https://doi.org/10.1016/j.msec.2019.109937>
33. Q. Nawaz et al., Bioactive glass based scaffolds incorporating gelatin/manganese doped mesoporous bioactive glass nanoparticle coating. *Ceram. Int.* **45**(12), 14608–14613 (2019). <https://doi.org/10.1016/j.ceramint.2019.04.179>
34. S. Fagerlund, L. Hupa, Crystallization of 45S5 during isothermal heat treatment. *Ceram Mater.* **62**, 349–354 (2009)
35. Q. Fu, E. Saiz, N. Rahaman, A. Tomsia, Bioactive glass scaffolds for bone tissue engineering: state of the art and future perspectives. *Mater. Sci. Eng. C Mater. Biol. Appl.* **31**, 1245–1256 (2011). <https://doi.org/10.1016/j.msec.2011.04.022>
36. M. Brink, T. Turunen, R. Happonen, A. Yli-Urpo, Compositional dependence of bioactivity of glasses in the system Na₂O–K₂O–MgO–CaO–B₂O₃–P₂O₅–SiO₂. *J. Biomed. Mater. Res.* **37**, 114–121 (1997). [https://doi.org/10.1002/\(SICI\)1097-4636\(199710\)37:1%3c114::AID-JBM14%3e3.0.CO;2-G](https://doi.org/10.1002/(SICI)1097-4636(199710)37:1%3c114::AID-JBM14%3e3.0.CO;2-G)
37. F. Westhauser et al., Bioactive Glass (BG) ICIE16 shows promising osteogenic properties compared to crystallized 45S5-BG. *Int. J. Mol. Sci.* (2020). <https://doi.org/10.3390/ijms21051639>
38. L. Aalto-Setälä, P. Uppstu, P. Sinityna, N.C. Lindfors, L. Hupa, Dissolution of amorphous S53P4 glass scaffolds in dynamic in vitro conditions. *Materials* (2021). <https://doi.org/10.3390/ma14174834>
39. J.R. Jones, Review of bioactive glass: from Hench to hybrids. *Acta Biomater.* **9**(1), 4457–4486 (2013). <https://doi.org/10.1016/j.actbio.2012.08.023>
40. M.J. Peltola, K.M.J. Aitasalo, J. Suonpää, A. Yli-Urpo, In Vivo model for frontal sinus and calvarial bone defect obliteration with bioactive glass S53P4 and hydroxyapatite. *J. Biomed. Mater. Res.* **58**, 261–269 (2001). [https://doi.org/10.1002/1097-4636\(2001\)58:33.3.CO;2-0](https://doi.org/10.1002/1097-4636(2001)58:33.3.CO;2-0)
41. H. Oonishi et al., Quantitative comparison of bone growth behavior in granules of bioglass, A-W glass-ceramic, and hydroxyapatite. *J. Biomed. Mater. Res.* **51**, 37–46 (2000). [https://doi.org/10.1002/\(SICI\)1097-4636\(200007\)51:1%3c37::AID-JBM6%3e3.0.CO;2-T](https://doi.org/10.1002/(SICI)1097-4636(200007)51:1%3c37::AID-JBM6%3e3.0.CO;2-T)

42. N. Lindfors, I. Koski, J.T. Heikkilä, K. Mattila, A.J. Aho, A prospective randomized 14-year follow-up study of bioactive glass and autogenous bone as bone graft substitutes in benign bone tumors. *J. Biomed. Mater. Res. B Appl. Biomater.* **94B**(1), 157–164 (2010). <https://doi.org/10.1002/jbm.b.31636>
43. O.P. Filho, G.P. La Torre, L.L. Hench, Effect of crystallization on apatite-layer formation of bioactive glass 45S5. *J. Biomed. Mater. Res.* **30**(4), 509–514 (1996). [https://doi.org/10.1002/\(SICI\)1097-4636\(199604\)30:4%3c509::AID-JBM9%3e3.0.CO;2-T](https://doi.org/10.1002/(SICI)1097-4636(199604)30:4%3c509::AID-JBM9%3e3.0.CO;2-T)
44. O. Peitl, E. Zanotto, L. Hench, Highly bioactive P2o5-Na2o-Cao-Sio2 glass-ceramics. *J. Non-Cryst. Solids* **292**, 115–126 (2001). [https://doi.org/10.1016/S0022-3093\(01\)00822-5](https://doi.org/10.1016/S0022-3093(01)00822-5)
45. J. Massera, S. Fagerlund, L. Hupa, M. Hupa, L. Pinckney, Crystallization mechanism of the bioactive glasses, 45S5 and S53P4. *J. Am. Ceram. Soc.* **95**, 607–613 (2012). <https://doi.org/10.1111/j.1551-2916.2011.05012.x>
46. S. Fagerlund, J. Massera, N. Moritz, L. Hupa, M. Hupa, Phase composition and in vitro bioactivity of porous implants made of bioactive glass S53P4. *Acta Biomater.* **8**(6), 2331–2339 (2012). <https://doi.org/10.1016/j.actbio.2012.03.011>
47. L. Lefebvre, L. Gremillard, J. Chevalier, R. Zenati, D. Bernache-Assolant, Sintering behaviour of 45S5 bioactive glass. *Acta Biomater.* **4**(6), 1894–1903 (2008). <https://doi.org/10.1016/j.actbio.2008.05.019>
48. T. Kokubo, H. Kushitani, S. Sakka, T. Kitsugi, T. Yamamuro, Solutions able to reproduce in vivo surface-structure changes in bioactive glass-ceramic A-W3. *J. Biomed. Mater. Res.* **24**(6), 721–734 (1990). <https://doi.org/10.1002/jbm.820240607>
49. D. Zhang, M. Hupa, H.T. Aro, L. Hupa, Influence of fluid circulation on in vitro reactivity of bioactive glass particles. *Mater. Chem. Phys.* **111**(2), 497–502 (2008). <https://doi.org/10.1016/j.matchemphys.2008.04.055>
50. O. Bretcanu, X. Chatzistavrou, K. Paraskevopoulos, R. Conradt, I. Thompson, A. Boccaccini, Sintering and crystallisation of 45S5 bioglass (R) powder. *J. Eur. Ceram. Soc.* **29**, 3299–3306 (2009). <https://doi.org/10.1016/j.jeurceramsoc.2009.06.035>
51. H. Arstila, L. Hupa, K. Karlsson, M. Hupa, In vitro bioactivity of partially crystallised glasses. *Glass Technol. Eur. J. Glass Sci. Technol. A* **48**, 196–199 (2007)
52. D. Rohanová, D. Horkavcová, A. Helebrant, A.R. Boccaccini, Assessment of in vitro testing approaches for bioactive inorganic materials. *J. Non-Cryst. Solids* **432**, 53–59 (2016). <https://doi.org/10.1016/j.jnoncrysol.2015.03.016>
53. M. Bohner, J. Lemaître, Can bioactivity be tested in vitro with SBF solution? *Biomaterials* **30**(12), 2175–2179 (2009). <https://doi.org/10.1016/j.biomaterials.2009.01.008>
54. L.L. Hench, D.E. Clark, Physical chemistry of glass surfaces. *J. Non-Cryst. Solids* **28**(1), 83–105 (1978). [https://doi.org/10.1016/0022-3093\(78\)90077-7](https://doi.org/10.1016/0022-3093(78)90077-7)
55. M. Cerruti, D. Greenspan, K. Powers, Effect of pH and ionic strength on the reactivity of Bioglass® 45S5. *Biomaterials* **26**(14), 1665–1674 (2005). <https://doi.org/10.1016/j.biomaterials.2004.07.009>
56. J.R. Jones, L.L. Hench, Biomedical materials for new millennium: perspective on the future. *Mater. Sci. Technol.* **17**(8), 891–900 (2001). <https://doi.org/10.1179/026708301101510762>
57. V. Mouriño, J.P. Cattalini, A.R. Boccaccini, Metallic ions as therapeutic agents in tissue engineering scaffolds: an overview of their biological applications and strategies for new developments. *J. R. Soc. Interface* **9**(68), 401–419 (2012). <https://doi.org/10.1098/rsif.2011.0611>